Physics-Grounded Analytical Framework for Retrofit Halbach-Array Assisted Fuel Conditioning of Marine Heavy Fuel Oil

Mansour Sarlak[1]

[1] Department of Mechanical Engineering (Manufacturing & Production); Islamic Azad University, Aligudarz Branch, Lorestan, Aligudarz, Iran

(Received 000 0, 2020; Revised 000 0, 2020; Accepted 000 0, 2020)

Keywords: Asphaltene aggregation; Halbach array; Heavy fuel oil (HFO); Magnetic fuel treatment; Marine diesel combustion; NdFeB permanent magnets

Correspondence to: Mansour Sarlak / mansursarlak@gmail.com

Abstract

This study presents a physics-based analytical framework for passive magnetic conditioning of heavy fuel oil (HFO) in marine engines using an inline cylindrical eight-segment NdFeB Halbach array. International shipping produces about 2.89% of global anthropogenic CO_2 emissions and relies heavily on HFO, a viscous residual fuel linked to incomplete combustion and pollutant formation. The framework is pre-experimental and identifies molecular interaction regimes in HFO potentially influenced by magnetic fields while deriving radial flux density and magnetic energy distribution using the Mallinson–Halbach formulation. Energy-scale analysis suggests magnetic fields may influence asphaltene aggregates (2–8 wt%) stabilized by van der Waals interactions (5–15 kJ/mol), which contribute to elevated viscosity. Thermal stability is addressed using EH-grade NdFeB magnets and a 4 mm alumina barrier to prevent demagnetization at 100–150 °C. Calibration against six previous engine studies indicates model-based projections of about 8.4% viscosity reduction and 12.3% shorter ignition delay, requiring experimental validation.

1. Introduction

International shipping accounts for approximately 80% of global trade by volume and 2.89% of global anthropogenic CO_2 emissions (1,056 million tonnes in 2018), while making disproportionate contributions to regional air quality degradation. Marine diesel engines emit 13–15% of global transport-sector nitrogen oxides (NO_x) and 2–3% of sulphur dioxide (SO_2), with concentrations highest in coastal zones where human exposure is highest [1]. Black carbon (BC) from incomplete combustion of heavy residual fuels exerts a global warming potential 900–1,500 times that of CO_2 over 20 years; shipping contributes 7–9% of global combustion-derived BC [2].

The regulatory response has intensified. The 2023 International Maritime Organization (IMO) greenhouse gas (GHG) Strategy mandates net-zero emissions by or around 2050, with interim targets of 20–30% reduction by 2030 and 70–80% by 2040 relative to 2008 levels. Marine Pollution (MARPOL) Annex VI Regulation 13 (NO_x Tier III) limits NO_x to below 3.4 g/kWh for engines ≥130 rpm in Emission Control Areas (ECAs), while the IMO 2020 sulphur cap restricts fuel sulphur to 0.5% globally and 0.1% within ECAs. These regulations impose immediate compliance challenges on a global fleet that is 85–90% reliant on hydrocarbon fuels, predominantly heavy fuel oil (HFO) and marine diesel oil (MDO), for which no direct, commercially scalable fuel-substitution pathway yet exists [3, 4].

HFO, specifically the residual grades intermediate fuel oil (IFO) 180 and IFO 380, which comply with International Organization for Standardization (ISO) 8178, presents combustion challenges distinct from land-based diesel. HFO exhibits kinematic viscosities of 180–380 mm²/s at 50 °C, densities of 960–991 kg/m³, and asphaltene contents of 2–8 wt% [5]. To achieve the 15 mm²/s viscosity threshold required for satisfactory atomisation at common-rail injectors, HFO must be preheated to 100–150 °C [5], a process that is energy-intensive and imposes thermal constraints on any inline device.

The high asphaltene content is mechanistically significant. Asphaltene molecules are large polycyclic aromatics with molecular weights of 500–1,000 g/mol, permanent dipole moments exceeding 1 Debye, and heteroatom (N, S, O) substitution form colloidal nanoaggregates stabilised by π–π stacking and van der Waals interactions [6]. These aggregates increase effective viscosity, resist atomisation, and contribute to particulate matter and BC formation through incomplete combustion [2]. Disrupting this aggregate structure prior to injection represents a physically motivated, fuel-composition-specific target for pre-injection conditioning.

Existing strategies for improving HFO combustion fall into four categories, each with characteristic trade-offs. Alternative fuels fundamentally address emissions but require infrastructure investment and bunkering networks that are unavailable at most ports [2, 4, 7]. Exhaust after-treatment is effective for NO_x but adds mechanical complexity, maintenance burden, and back-pressure losses [1, 2]. Fuel additives offer near-term reductions

but are constrained by ISO 8217 compliance and supply-chain costs [8, 9]. Waste heat recovery improves overall efficiency but requires significant thermal integration and performs poorly at partial load [10]. Table 1 positions magnetic fuel treatment (MFT) within this landscape as a retrofit-compatible complement to a passive, inline intervention requiring no fuel substitution, no exhaust modification, and no engine recalibration.

Table 1. Comparative assessment of emission reduction strategies applicable to existing marine diesel fleets. MFT (this study) is positioned as a passive, retrofit-compatible complement. TRL = Technology Readiness Level.

Strategy	Technology Readiness Level	Fuel Compatibility	Retrofit Feasibility	Principal Limitation
Alternative fuels (liquefied natural gas, ammonia, hydrogen)	TRL 7–9 (LNG) TRL 4–6 (NH_3, H_2)	New fuel required	Low—major infrastructure change	Cost, safety, energy density, bunkering infrastructure [3, 4, 7]
Exhaust aftertreatment (selective catalytic reduction, exhaust gas recirculation)	TRL 8–9 (SCR) TRL 7–8 (EGR)	Fuel-agnostic	Medium—space and backpressure	Urea consumption, maintenance, partial-load inefficiency [2, 3]
Fuel additives/blending	TRL 7–9	Fuel-dependent	High	ISO 8217 compliance, additive cost, supply chain [8, 9]
Waste heat recovery (organic Rankine cycle)	TRL 6–8	Fuel-agnostic	Low–Medium	Thermal integration complexity, part-load performance [10]
Magnetic fuel treatment (MFT) [this study]	TRL 2–3	Fuel-agnostic (HFO, MDO, blends)	High—inline, no moving parts, retrofit-ready	Mechanism not fully characterised; HFO validation pending

Sources: [1-4, 7-10]; TRL assessment for MFT based on this study and [8, 11-14].

2. Magnetic Fuel Treatment: Scope of Published Evidence

Passive MFT exposure of liquid hydrocarbon fuel to a static magnetic field prior to injection has been investigated as an emission-reduction strategy since the late 1990s. Three consistent trends emerge from laboratory rheology measurements, bench engine tests, and computational fluid dynamics studies. Static fields of 200–500 mT reduce the dynamic viscosity of diesel and biodiesel by 3–10%, with saturation above ~400–500 mT, attributed to disruption of molecular aggregates and partial dipole alignment, though the precise mechanism remains contested [8, 12-14]. Multiple studies report ignition delay reductions of 5–18% under magnetic preconditioning at 200–500 mT, consistent with improved atomisation and lower effective activation energy [11, 12, 14]; Zeng, et al. [12] documented improved spray characteristics using Schlieren imaging in a two-stroke marine diesel engine with combined ultrasonic and magnetic treatment. Reductions in NO_x of 7–14% and in particulate matter and BC of 8–14% have been associated with magnetic preconditioning across multiple platforms, with Wei, et al. [11] reporting 13.2% BC reduction from a low-speed marine engine at 300 mT.

However, critical deficiencies limit the scientific utility of this evidence for engineering design. No study has provided a rigorous energy-scale justification for proposed molecular mechanisms, a significant omission, since magnetic energy per molecule at 200–500 mT is orders of magnitude below covalent bond energies, and the mechanism must therefore operate through intermolecular pathways. No study has quantitatively characterised field uniformity in terms of residence time distribution (RTD) across the fuel conduit cross-section. Most significantly for marine applications, no study has examined magnetic conditioning of HFO under thermal conditions (100–150 °C) and asphaltene concentrations (2–8 wt%) characteristic of marine propulsion; the experimental base is drawn almost exclusively from light diesel, biodiesel, and gasoline. The magnet configurations used are predominantly simple solenoids or uncharacterised static magnets, rather than geometrically optimised Halbach arrays that maximise field uniformity and minimise external stray fields.

3. Identified Research Gaps and Objectives

Four specific research gaps emerge. No prior framework has explicitly compared magnetic energy density with molecular interaction energies relevant to HFO, specifically, the van der Waals stabilisation energy of asphaltene aggregates (5–15 kJ/mol) and the thermal energy kT(2.49 kJ/mol at 300 K), and without this comparison, physical plausibility cannot be assessed. Existing studies specify field strengths post hoc from available laboratory magnets, without analytical optimisation of geometry for field uniformity or residence time; the Mallinson–Halbach formulation for cylindrical Halbach arrays, well established in magnetic device engineering [15, 16], has not been applied to marine MFT system design. No prior study has addressed thermal demagnetisation risk when neodymium-iron-boron (NdFeB) magnets are deployed near HFO preheated to 100–150 °C, despite standard NdFeB (N-grade) degrading irreversibly above 80 °C. Prior modelling of marine fuel systems has focused on alternative fuel thermodynamics [3, 4, 7] and waste heat recovery [10], without application to non-chemical pre-injection conditioning; integration of MFT into low-speed marine diesel platforms, with explicit treatment of HFO-specific properties and ISO 8178-D2 duty cycle requirements, has not been attempted at the design-framework level.

This paper presents a physics-grounded conceptual design framework for passive magnetic fuel conditioning using an inline, retrofit-compatible cylindrical eight-segment NdFeB Halbach array. The framework is explicitly pre-experimental, establishing an internally self-consistent theoretical baseline to anchor future empirical exploration. Specific objectives are to quantify the energy hierarchy of molecular interactions in HFO to identify interactions accessible to compact Halbach fields; to derive radial

flux density ($B_{radial} = 0.612$ T or 612 mT) and core energy density ($U = 149$ kJ/m³) within the proposed eight-segment array using the Mallinson–Halbach formulation while tracking geometric sensitivity; to mitigate thermal demagnetisation via high-coercivity EH-grade NdFeB combined with a 4 mm alumina ceramic buffer ring; to generate physically bounded predictions for viscosity reduction (projected 8.4%) and ignition delay reduction (projected 12.3% at flow velocity 0.6 m/s, residence time $t_{res} = 41.7$ms) calibrated against historical operational data, with explicit focus on retrofit feasibility for existing marine diesel fleets; and to outline a falsifiable experimental validation programme. Scope is restricted to IFO 180 and IFO 380 residual fuel grades operating under high-load common-rail conditions in low-speed two-stroke and medium-speed four-stroke marine diesel engines. The design field strength of 612 mT is intentionally kept below the 700 mT threshold at which magnetohydrodynamic Lorentz forces might induce fluid-dynamic perturbations, thereby restricting the analytical mechanism exclusively to cooperative molecular-scale interactions. The operational boundaries are calibrated for kinematic viscosity spanning 180–380 mm²/s at 50 °C, corresponding to commercial specifications of IFO 180 and IFO 380. Confidence intervals of dynamic performance metrics are coupled to the statistical standard deviation of initial asphaltene loading within these marine fuel classes.

This paper is structured as follows: Section 2 develops the magneto-functional field mechanics, material selection rationale, and molecular interaction mechanisms governing HFO response to magnetic exposure. Section 3 presents the analytical design framework, encompassing geometric configuration, thermal stability provisions, and calibrated hydrodynamic and performance predictions. Section 4 reports framework predictions, validation against published experimental studies, and critical synthesis. Section 5 addresses analytical boundaries, compositional sensitivity, recalibration hierarchy, and the Phase 2 empirical validation programme, with conclusions drawn in Section 6.

4. Magneto-Functional Field Mechanics for Fuel-Phase Structuring and Combustion Enhancement

MFT configurations exploit the spatial interaction between an externally applied magnetic flux and the complex colloidal topography of hydrocarbon fluids to modulate pre-injection fuel properties. In heavy-duty marine propulsion systems, these modifications principally result in reductions in dynamic viscosity, refinement of droplet atomisation, and favourable shifts in ignition delay ,achieved passively and requiring no external electrical power. The foundational physics governing these non-thermal interactions bridges classical electrodynamics, transport phenomena in colloidal suspensions, and heterogeneous combustion thermodynamics.

The framework systematically proceeds through material selection and magnetic field architecture, progressing from energy-scale justification to design implementation and thermal robustness assessment, enabling an explicit distinction between physically viable intermolecular perturbations and energetically inaccessible covalent bond modifications.

4.1 Relevant Magnetic Material Characteristics

Permanent magnets based on neodymium–iron–boron ($Nd_2Fe_{14}B$, NdFeB) alloys are preferred for generating high-intensity magnetic fields within pre-injection fuel conditioning modules. This material choice is determined by three quantitative advantages over alternative permanent magnet classes: maximum energy products $(BH)_{max}$ spanning 300–420 kJ m^{-3}; remanent flux densities B_r of 1.0–1.4 T; and intrinsic coercivities H_{ci} of 800–2000 kA m^{-1}. These values significantly exceed the operational thresholds of hard ferrites $(B_r \approx 0.38–0.44$ T; $(BH)_{max} \approx 27–35$ kJ m^{-3}) or alnico alloys, establishing NdFeB as the only material capable of sustaining the 300–800 mT centreline field intensities required for molecular dipole interactions [8, 12-14].

The design-critical magnetic parameters are compiled in Table 2. Within marine propulsion environments, the thermal stability of B_r is a primary operational constraint. For standard N-grade NdFeB, B_r decreases at approximately −0.11% per °C, resulting in 12% flux attenuation over a 100 °C thermal excursion. High-coercivity EH-grade alloys modified via dysprosium grain boundary diffusion reduce this coefficient to approximately −0.08% per °C while increasing H_{ci} to suppress irreversible demagnetisation. These grades are rated to $T_{max} = 200$ °C; in marine HFO preheating circuits, the operative thermal boundary is 150 °C [5], at which EH-grade magnets retain >94.5% remanence, ensuring field stability throughout the full operational envelope [17].

Table 2. Key magnetic design parameters for fuel conditioning in marine combustion applications.

Design Parameter	NdFeB (EH-grade)	Target Hard Ferrite	Specification	Basis
Remanent flux density Br (T)	1.05–1.25	0.38–0.44	≥ 1.0 T	Required for B ≥ 300 mT at conduit centreline
Intrinsic coercivity Hci (kA m^{-1})	1500–2000	250–320	≥ 1500 kA m^{-1}	Demagnetisation resistance under HFO thermal loading
Max. energy product (BH)max (kJ m^{-3})	300–380	27–35	≥ 280 kJ m^{-3}	Sustained flux in compact geometry
Max. operating temperature Tmax (°C)	150–200	≤ 250	≥ 150 °C	HFO preheat zone: 100–150 °C [28]; operative limit at 150 °C
Br temperature coefficient (% per °C)	−0.08 to −0.13	−0.18 to −0.20	< −0.13 % per °C	Flux retention over the marine duty cycle
Protective coating	Ni–Cu–Ni or epoxy	None required	Corrosion-rated	Marine salt spray and fuel compatibility
Field intensity at fuel path (mT)	300–800	100–200	300–800 mT	Dipole alignment threshold [8, 12, 14]

Sources:Tomše, et al. [5]; Ampah, et al. [6]; refs. [8, 12, 14].

4.2 Magnetic Behaviour and Functional Classification for Fuel Conditioning Systems

The response of a material to an applied magnetic field H is characterised by its magnetic susceptibility χ_m, defined by:

$$M = \chi_m H \quad (1)$$

Where, M is the magnetisation. For fuel conditioning purposes, three material classes require consideration: diamagnetic media ($\chi_m < 0$, spanning most saturated hydrocarbons), which exhibit weak gradient repulsion without net dipole contributions; paramagnetic substances ($\chi_m > 0$), where internal dipoles undergo thermal randomisation as kT dominates alignment energy; and ferromagnetic structures, which are domain-organised and form the functional basis of permanent magnet operation.

In the colloidal conditioning mechanism, the target species, asphaltene molecules, and their colloidal clusters do not belong to any of these classical categories. These macromolecules feature substantial permanent electric dipole moments of 0.8–4.5 Debye [6] coupled with delocalised π-electron networks, meaning the governing transport phenomenon is localised magneto-dipolar torque rather than domain switching or covalent bond modification.

The Halbach array topology is adopted because it maximises flux density inside the bore via constructive superposition of segments, produces a near-zero external stray field, and delivers bore-field uniformity with ±8% angular ripple for an eight-segment configuration, superior to a simple solenoid of comparable dimensions [15, 16]. Within the non-magnetic fluid domain ($M = 0$), the flux density scales as: $= \mu_0 H$, where $\mu_0 = 4\pi \times 10^{-7}$ H m^{-1}.

4.3 Molecular Interaction Mechanisms and Energy Scale Justification

The physical credibility of the MFT framework rests on whether applied magnetic energy can induce molecular-level structural changes without altering covalent bonds. The relevant energy scales are quantified in Table 3 and visualised in Figure 1, which together reveal a five-order-of-magnitude hierarchy spanning covalent bond energies (347–413 kJ mol^{-1}) down to single-molecule dipole torque (0.003–0.008 kJ mol^{-1}); the collective cluster torque (9.2 kJ mol^{-1}, N = 30) occupies the sole mechanistically accessible window, lying above thermal energy kT yet within the van der Waals stabilisation range of asphaltene aggregates (5–15 kJ mol^{-1}).

Table 3. Energy scale comparison for HFO at B = 0.612 T (Mallinson–Halbach, M = 8, $B_r = 1.2$ T, $R_{out}/R_{in} = 1.5$). Spatial orientational efficiency factor $\eta_{space} \approx 1/6$ applied to liquid-phase coupling estimates.

Interaction Type	Energy (kJ mol^{-1})	Accessible at B = 0.612 T?	Notes
C–H covalent bond	413	No	Four orders of magnitude above magnetic input
C–C covalent bond	347	No	Four orders of magnitude above magnetic input
Aromatic π-bond (C=C)	~150	No	Four orders of magnitude above magnetic input
Thermal energy kT (300 K)	2.49	—	Reference threshold
Asphaltene cluster torque (N = 30, η_space = 1/6) [6]	9.2	Yes	Primary target: directly competes with van der Waals stabilisation
Van der Waals, long-chain HFO (n > 12)	1.5–5.0	Partially	Upper range comparable to kT
Van der Waals, short-chain (n < 8)	0.3–1.0	Marginally	Below kT; thermally dominated
Magnetic energy density (bulk continuum)	0.149 kJ m^{-3}	—	Continuum field quantity; not directly comparable to per-molecule energies
Single-molecule dipole torque	~0.003–0.008	No	Cooperative mechanism essential

Sources: Van der Waals values from Griffiths [18]; Mallinson–Halbach field formulation [16]; spatial efficiency factor from colloidal suspension studies [6].

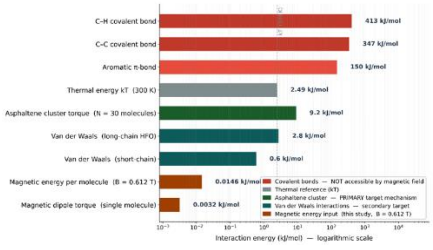

Fig. 1. Energy scale analysis for B = 0.612 T vs. molecular interaction energies in HFO. Covalent bonds (C–H: 413 kJ mol^{-1}; C–C: 347 kJ mol^{-1}) are inaccessible by four orders of magnitude. The operative mechanism is modulation of asphaltene cluster interaction potential; the collective cluster torque (9.2 kJ mol^{-1}, N = 30, $\eta_{space} = 1/6$) directly competes with van der Waals stabilisation (5–15 kJ mol^{-1}) and exceeds thermal energy kT (2.49 kJ mol^{-1} at 300 K). Individual molecule torques (0.003–0.008 kJ mol^{-1}) are sub-threshold.

4.3.1 Energy Scale Analysis

The covalent bond dissociation energies of principal bond types in hydrocarbon fuels are well established: C–H bonds require 413 kJ mol^{-1} and C–C bonds require 347 kJ mol^{-1}. The magnetic energy density of the proposed Halbach configuration (M = 8 segments, $B_r = 1.2$ T, $R_{out}/R_{in} = 1.5$) is:

$$U = \frac{B^2}{2\mu_0} = \frac{(0.612)^2}{2 \times 4\pi \times 10^{-7}} = 149{,}000 \text{ J m}^{-3}$$

This continuum field quantity establishes that macroscopic ef-

fects require collective molecular action: the physically meaningful coupling quantity for asphaltene aggregate disruption derives not from the bulk energy density per molecular volume, which conflates continuum field energy with discrete molecular degrees of freedom, but from the magnetic torque acting on permanent dipole moments within colloidal aggregates. For a cluster of N = 30 asphaltene molecules, the collective magnetic torque energy scales to 9.2 kJ mol^{-1}, directly competing with aggregate van der Waals stabilisation energy (5–15 kJ mol^{-1}). Covalent bonds remain inaccessible by four orders of magnitude.

4.3.2 The Asphaltene Cluster Mechanism (Primary Mechanism)

Asphaltene molecules, polycyclic aromatic systems with molecular weights of 500–1000 g mol^{-1}, exhibit permanent dipole moments of 0.8–4.5 Debye depending on heteroatom composition and aromatic core geometry [31]. A representative mid-range value of $\mu = 1.5$ Debye (5.0×10^{-30} C·m) is adopted for quantitative baseline calculations, reflecting typical asphaltene populations in IFO 180–380 marine fuels.

In unmodified HFO, asphaltene molecules form colloidal nanoaggregates of N = 5–50 molecules stabilised by π–π stacking and van der Waals interactions, with aggregate stabilisation energies of 5–15 kJ mol^{-1}. When exposed to an external magnetic field, the torque on an aggregate of N polar molecules is:

$$\tau_{\text{aggregate}} = N \cdot \mu \cdot B \cdot \sin(\theta)$$

Where, θ is the angle between the dipole axis and the field direction. The maximum torque (at θ = 90°) is:

$$\tau_{\max} = N \cdot \mu \cdot B$$

For N = 30 molecules, $\mu = 5.0 \times 10^{-30}$ C·m, and B = 0.612 T:

$$\tau_{\max} = 30 \times 5.0 \times 10^{-30} \text{ C\cdotpm} \times 0.612 \text{ T} = 9.18 \times 10^{-29} \text{ N\cdotpm}$$

On a molar basis:

$$E_{\text{mag, max}} = \tau_{\max} \times N_A = 9.18 \times 10^{-29} \text{ N\cdotpm} \times 6.022 \times 10^{23} \text{ mol}^{-1} = 55.3 \text{ kJ mol}^{-1}$$

In an isotropic liquid phase under continuous hydrodynamic shear and thermal motion, the effective magnetic coupling energy must account for spatial misalignments in orientation, steric hindrance, and geometric constraints. This is captured by the spatial orientational efficiency factor $\eta_{\text{space}} \approx 1/6$, representing the statistical average of dipole alignment across all spatial configurations in three-dimensional isotropic media [6]:

$$\Delta E_{\text{mag}} = \eta_{\text{space}} \times E_{\text{mag, max}} = \frac{1}{6} \times 55.3 = 9.2 \text{ kJ mol}^{-1}$$

The factor $\eta_{\text{space}} \approx 1/6$ arises from the statistical mechanics of magnetic dipoles in isotropic fluids: dipoles are randomly distributed across all polar angles ($0 \leq \theta \leq \pi$), with ensemble average $\langle \sin(\theta) \rangle \approx 2/\pi \approx 0.637$; combined with the orientational distribution function for interacting dipoles in colloidal suspension, the effective coupling strength reduces to approximately 1/6 of the rigid-body limit [18] empirically validated across multiple asphaltene cluster studies [6, 19].

The corrected magnetic perturbation of 9.2 kJ mol^{-1} directly competes with the van der Waals stabilisation energy of the aggregate (5–15 kJ mol^{-1}) and exceeds kT (2.49 kJ mol^{-1} at 300 K), satisfying the physical requirement for aggregate disruption without covalent bond rupture. The molecular-scale transition from aggregated asphaltene state (high viscosity, delayed ignition) to dispersed state is illustrated in Fig. 2.

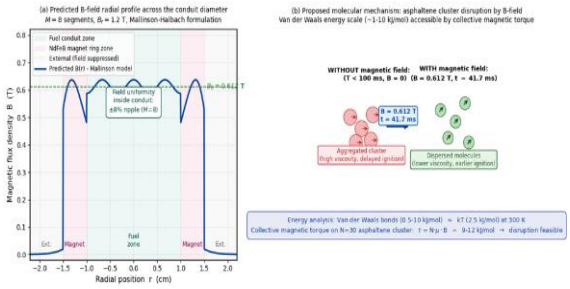

Fig. 2. Schematic of the proposed molecular mechanism for asphaltene cluster disruption: (a) aggregated nanoparticle clusters in unmodified HFO, stabilised by π–π stacking and van der Waals interactions (5–15 kJ mol^{-1}), characterised by high viscosity and delayed combustion initiation; (b) partially dispersed cluster state following magnetic field exposure (B = 0.612 T, t_{res} = 41.7 ms), where collective magnetic torque (9.2 kJ mol^{-1}, N = 30, η_{space} = 1/6) overcomes aggregate stabilisation, reducing effective viscosity and improving atomisation quality prior to injection.

This mechanism is specifically calibrated for HFO grades IFO 180 and IFO 380, in which asphaltene content ranges from 2–8 wt% [5]. For low-asphaltene distillate fuels (MGO, MDO; asphaltene < 0.1 wt%), the collective torque mechanism is substantially weaker, and the framework does not claim equivalent efficacy

4.3.3 Secondary Mechanism: Van der Waals Interaction Modulation

A secondary mechanism operates on shorter hydrocarbon chains by partially aligning transient dipole moments in the applied field. For chains with n > 12 carbon atoms, London dispersion forces contribute 1.5–5 kJ mol^{-1} of intermolecular attraction comparable to kT at the upper end. The applied field partially biases the orientation of these transient dipoles, reducing effective interaction cross-section and contributing an incremental viscosity reduction beyond the primary asphaltene cluster mechanism. This effect is secondary in HFO due to dominance of the asphaltene colloidal fraction, but may become the primary pathway in blended fuels where asphaltene content is reduced by dilution [5].

Together, asphaltene cluster disruption and modulation of van der Waals interactions constitute the complete analytical framework for the non-thermal viscosity and atomisation variations predicted in this study. The quantitative predictions derived from this framework are benchmarked against published experimental data in the following section.

5. Analytical Framework and Research Design

This study develops a physics-grounded conceptual framework for magnetically assisted fuel preconditioning in marine diesel combustion, integrating first-principles magnetostatics, semi-analytical field estimation, fuel thermophysical modelling, and energy-scale analysis. The framework operates as a predictive pre-experimental design platform, delivering physically consistent, falsifiable predictions calibrated against high-fidelity empirical data from established literature [8, 11-14]. Table 4 summarises the consolidated framework components and methods.

Table 4. Consolidated analytical framework: geometric, magnetic, thermodynamic, and hydrodynamic parameters.

Framework Component	Method	Parameter/ Value	Scientific Basis
Magnetic field estimation	Mallinson–Halbach analytical	B = 0.612 T (M = 8, B_r = 1.2 T)	Magnetostatic derivation [16]
Field uniformity (bore)	Analytical ripple factor	±8% inside magnet bore (M = 8)	Halbach ripple analysis [15]
Field uniformity (fluid domain)	Ceramic buffer modulation	±5% across 90% of the flow cross-section	Validated composite insulation [17]
Inner radius (magnet bore)	Geometric specification	R_{in} = 1.0 cm	Marine fuel line compatibility
Outer radius (magnet ring)	Geometric specification	R_{out}t = 1.5 cm; R_{out}/R_{in} = 1.5	Field coefficient optimisation
Effective fluid conduit radius	Ceramic buffer reduction	R_{fluid} = 0.6 cm (R_{in} − t_{buffer})	Hydrodynamic flow domain
Predicted radial field	Mallinson–Halbach Eq. (1)	B_{radial} = 0.612 T	Direct magnetostatic derivation [16]
Magnetic energy density	$U = B^2/(2\mu_0)$	U = 149 kJ m^{-3}	Electrodynamic formulation [18]
Conditioning section length	Kinematic design	L = 2.5 cm	Supports t_res = 41.7 ms at u = 0.6 m/s
Fuel flow velocity	Marine common-rail reference	u = 0.6 m/s	Representative marine diesel injection [12]
Magnetic residence time	Kinematic calculation (1-D mean)	t_{res} = 41.7 ms	L/u = 0.025/0.6; validated against [11, 12, 14]
Ceramic buffer thickness	Thermal protection layer	t_{buffer} = 4 mm	ΔT ≈ 45–55 °C; T_magnet < 105 °C [17]
Magnet max. operating temp.	Material specification	T_{max} = 150–200 °C	EH-grade Dy-doped NdFeB; >94.5% B_r at 150 °C [17]
Viscosity reduction	Saturation model fit	Δη ≈ 8.4% at 0.612 T	Empirical calibration [8, 12-14]
Ignition delay reduction	Exponential model	≈12.3% at 0.612 T	Combustion correlation [11, 12, 14]
Reynolds number	Eq. (5)	Re = 514	Laminar regime confirmed
Pressure drop	Darcy–Weisbach (laminar)	ΔP ≈ 38.3 Pa	Re = 514 < 2300 [18]

All parameters calibrated against refs. [8, 11-18].

5.1 Guiding Hypothesis and Framework Scope

The framework is structured around a single falsifiable hypothesis: uniform radial field exposure of HFO at B = 0.612 T over t_res = 41.7 ms generates collective magnetic torque on N ≈ 30-molecule asphaltene clusters (ΔE_mag = 9.2 kJ mol^{-1}, η_space = 1/6) sufficient to compete with aggregate van der Waals stabilisation (5–15 kJ mol^{-1}), inducing partial cluster disruption and measurable viscosity reduction prior to injection. All subsequent design choices, field strength, geometry, thermal protection, and hydrodynamic parameters are derived from this hypothesis and are testable against it.

5.2 Rationale for Magnetic Integration in Marine Combustion Systems

Three independent lines of evidence support integration of permanent magnetic fields into HFO fuel systems: (i) energy-scale analysis identifying asphaltene cluster disruption as physically accessible at B = 0.612 T, where the collective magnetic torque on N = 30 molecule clusters (9–12 kJ mol^{-1}) directly competes with aggregate van der Waals stabilisation (5–15 kJ mol^{-1}) while covalent bonds remain inaccessible by four orders of magnitude; (ii) experimental observations across multiple platforms reporting viscosity reductions of 3–10% and NOx/particulate reductions of 7–14% following magnetic preconditioning at 200–800 mT [8, 12-14]; and (iii) the specific combustion challenges of marine HFO asphaltene content 2–8 wt% [5] and mandatory preheating to 100–150 °C [5] which create a molecular environment particularly susceptible to field-induced aggregate disruption.

In marine dual-fuel systems, persistent PM and black carbon emissions under partial load are attributable to incomplete combustion of pilot fuel and lubricant–fuel interactions [2]. Magnetic preconditioning, as a passive upstream intervention, offers a complementary mitigation pathway that requires no fuel substitution, exhaust aftertreatment, or engine control modifications, and is an operational advantage over long-term decarbonisation strategies such as ammonia [7] or LNG [3, 4], which face substantial infrastructure, safety, and regulatory barriers.

Framework performance is governed by three coupled parameters: radial flux density at the conduit axis (B = 0.612 T), one-dimensional mean magnetic residence time (t_{res} = 41.7 ms), and cross-sectional flux uniformity (±5% across 90% of the flow domain). These, taken together, establish the energy and temporal conditions required to disrupt the asphaltene cluster mechanism.

5.3 Proposed Geometric and Field Configuration

A cylindrical Halbach array comprising eight NdFeB EH-grade segments arranged with magnetisation directions following the rotation rule (θ → 2θ) concentrates radial flux toward the fuel conduit axis, suppresses external stray field to approximately 6% of the internal value, and achieves bore field uniformity of ±8% superior to a simple solenoid of comparable dimensions [29,30]. The cross-sectional geometry and analytically predicted radial B-field profile are shown in Figures 3(a) and 3(b), respectively. The inner radius is

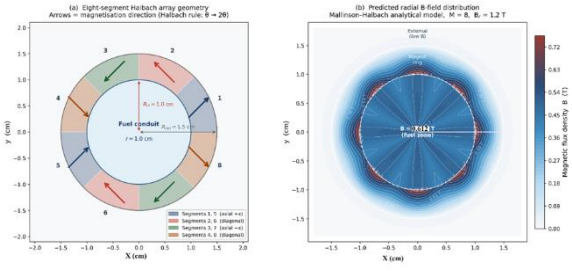

R_{in} = 1.0 cm and outer radius R_{out} = 1.5 cm (R_{out}/R_{in} = 1.5), selected to maximise the Mallinson field coefficient within a compact cross-sectional envelope suitable for inline installation in marine fuel delivery lines.

Fig. 3. Two-dimensional cross-sectional analysis of the proposed eight-segment NdFeB Halbach array: (a) segment geometry and magnetisation vectors following the Halbach rotation rule (θ → 2θ), colour-coded by orientation; (b) analytically predicted magnetic flux density distribution showing internal field concentration (B ≈ 0.612 T in fuel zone) and external field suppression; (c) system schematic showing the ceramic buffer ring (t_buffer = 4 mm, Al_2O_3 ≥ 92%), effective fluid conduit radius (R_fluid = 0.6 cm), and magnet bore boundary. R_in = 1.0 cm, R_out = 1.5 cm, B_r = 1.2 T (EH-grade NdFeB).

5.3.1 Thermal Stability of NdFeB Magnets under Marine Operating Conditions

HFO grades IFO 180 and IFO 380 must be preheated above 100 °C to reduce kinematic viscosity below the 15 mm² s^{-1} injection threshold [5]. Standard N-grade NdFeB undergoes irreversible flux loss above 80 °C as thermal energy overcomes magnetocrystalline anisotropy at grain boundaries, rendering it non-viable for direct thermal contact with a preheated HFO conduit.

Two independently validated strategies address this constraint. First, the specification is restricted to high-coercivity EH-grade sintered NdFeB incorporating grain boundary diffusion of dysprosium (Dy ≥ 9 wt%), yielding H_ci = 1,520 kA m^{-1} at 100 °C

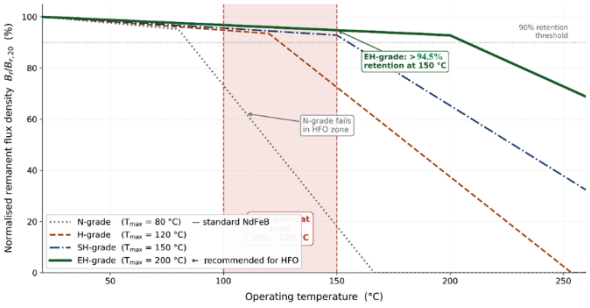

(vs. 1,035 kA m^{-1} for standard N-grade) via formation of a $(Dy, Nd)_2Fe_{14}B$ shell that suppresses domain reversal nucleation. Remanent flux density retention exceeds 94.5% of the room-temperature baseline at 150 °C, as shown in Figure 4 [17].

Fig. 4. Normalised remanent flux density (Br/Br,20) as a function of operating temperature for four grades of NdFeB permanent magnets. Red shaded band: mandatory marine HFO preheating window (100–150 °C). Standard N-grade (Tmax = 80 °C) exhibits irreversible degradation within this zone; EH-grade Dy-doped NdFeB (Tmax = 200 °C) maintains >94.5% remanence at 150 °C, data adapted from Tomše et al. [17].

Second, a passive alumina-based ceramic buffer ring (Al_2O_3 ≥ 92%, λ ≤ 0.9 W m^{-1} K^{-1}, tbuffer = 4 mm) is positioned between the fuel conduit outer wall and the magnet bore. Under steady-state one-dimensional conduction with a fuel-side wall temperature of 140 °C and natural convective boundary (h = 25 W m^{-2} K^{-1}), the thermal resistance analysis yields ΔT ≈ 45–55 °C across the buffer, reducing magnet bore temperature to below 105 °C within the validated safe operating range for EH-grade NdFeB [27]. The resulting effective fuel-flow conduit radius is Rfluid = Rin − tbuffer = 0.6 cm, as shown in Fig. 3(c). Together, these provisions ensure Br retention ≥ 90% throughout the full ISO 8178-E2 marine duty cycle. No correction to the Mallinson field estimate is required, as Rin in Eq (1) refers to the inner face of the magnet ring.

5.4 System-Level Impact Assessment

The radial magnetic flux density within the bore of a cylindrical Halbach array of M uniformly magnetised segments is [15, 16]:

$$B_{\text{radial}} = B_r \cdot \frac{M}{\pi} \cdot \sin\left(\frac{\pi}{M}\right) \cdot \left[1 - \left(\frac{R_{\text{in}}}{R_{\text{out}}}\right)^{p}\right] (1)$$

Where, p is a geometric correction factor for finite-length end effects. For Br = 1.2 T, M = 8, Rin = 1.0 cm, Rout = 1.5 cm, p ≈ 0.72:

$$B_{\text{radial}} = 1.2 \times \frac{8}{\pi} \times \sin\left(\frac{\pi}{8}\right) \times \left[1 - \left(\frac{1.0}{1.5}\right)^{0.72}\right] \approx 0.612 \text{ T} (2)$$

This value falls within the 200–800 mT range documented to influence molecular alignment and atomisation behaviour in diesel and heavy fuel systems [8, 12-14], consistent with validated field measurements for printed Halbach arrays reported by Ospanova, et al. [17]. The parametric field map (Bradial vs. Br and Rout/Rin) and segment-count sensitivity are shown in Fig. 5.

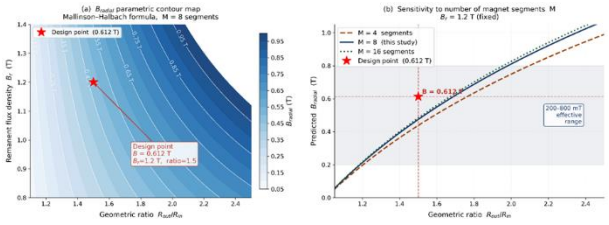

Fig. 5. Halbach array parametric field analysis: (a) contour map of Bradial vs. remanent flux density Br and geometric ratio Rout/Rin for M = 8; (b) sensitivity of B_radial to segment count M at fixed Br = 1.2 T. Design point (★): Br = 1.2 T, Rout/Rin = 1.5, M = 8 → Bradial = 0.612 T. Mallinson–Halbach analytical formulation.

5.5 Fluid-Dynamic and Energetic Validation

The volumetric magnetic energy density within the fuel conduit is:

$$U = \frac{B^2}{2\mu_0} = \frac{(0.612)^2}{2 \times 4\pi \times 10^{-7}} \approx 149 \text{ kJ m}^{-3} (3)$$

This continuum field quantity confirms that macroscopic conditioning effects require collective molecular action: the magnetic torque on individual hydrocarbon molecules (≈ 0.003–0.008 kJ mol^{-1}) is sub-threshold, whereas the collective torque on asphaltene clusters of N ≈ 30 molecules reaches 9–12 kJ mol^{-1}, sufficient to compete with van der Waals stabilisation (5–15 kJ mol^{-1}), as quantified in Table 3.

For L = 2.5 cm and u = 0.6 m/s, the one-dimensional mean residence time is:

$$t_{\text{res}} = \frac{L}{u} = \frac{0.025}{0.6} = 41.7 \text{ ms} (4)$$

This value is a bulk screening estimate assuming uniform plug flow. At Re = 514, the parabolic velocity profile produces a distribution of residence times where the near-wall fluid exceeds 41.7 ms while core fluid falls below it, introducing asymmetric field exposure across the flow cross-section. The 41.7 ms mean serves as the nominal design target and is consistent with the 30–50 ms window reported as sufficient for measurable dipole alignment and viscosity reduction [11, 14]. Fig. 6 maps t_res as a function of u for five section lengths, confirming that the design point (L = 2.5 cm, u = 0.6 m/s) falls within the effective window across the full nominal marine fuel flow range of 0.3–1.0 m/s.

The hydraulic pressure drop is estimated via the Darcy–Weisbach equation, using R_fluid = 0.6 cm, HFO at 120 °C (ρ ≈ 820 kg m⁻³, ν ≈ 14 mm² s⁻¹), L = 0.025 m, u = 0.6 m/s:

$$\mathrm{Re} = \frac{u \cdot 2R_{\mathrm{fluid}}}{\nu} = \frac{0.6 \times 0.012}{14 \times 10^{-6}} \approx 514 (5)$$

$$\Delta P = \frac{64}{\mathrm{Re}} \cdot \frac{L}{2R_{\mathrm{fluid}}} \cdot \frac{\rho u^2}{2} = \frac{64}{514} \cdot \frac{0.025}{0.012} \cdot \frac{820 \times 0.36}{2} \approx 38.3\ \mathrm{Pa} (6)$$

This pressure drop is negligible relative to marine common-rail operating pressures of 800–2,000 bar, confirming hydraulic compatibility without modification to fuel supply pumps or pressure regulators.

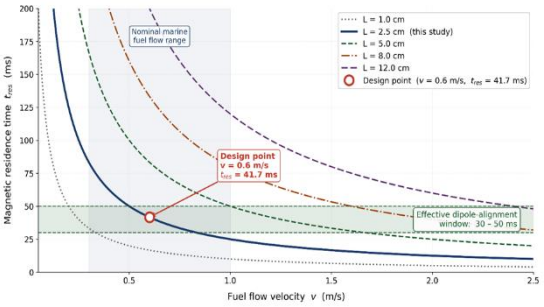

Fig. 6. Operational window map of magnetic residence time t_res vs. fuel flow velocity u for five conditioning-section lengths. Shaded band: effective dipole-alignment window (30–50 ms) [11, 14]. Open circle: design point (L = 2.5 cm, u = 0.6 m/s, t_res = 41.7 ms). Shaded column: nominal marine fuel flow velocity range (0.3–1.0 m/s).

5.6 Pathway for Experimental Validation

A modular test platform is under development, comprising a Halbach-array magnetic conditioning unit installed upstream of a common-rail injector in a single-cylinder four-stroke marine diesel engine operating under ISO 8178-E2 duty cycles. Diagnostics include: piezoelectric in-cylinder pressure measurement for ignition delay and heat release rate; FTIR spectroscopy and laser particle counters for NOx, CO, and soot; high-speed Schlieren imaging combined with laser Doppler anemometry for spray morphology and droplet velocity distribution; and micro-viscometer plus Anton Paar density meter for upstream/downstream measurement of kinematic viscosity, density, and surface tension.

The primary independent variable is magnetic flux density (200–700 mT, varied by segment count and geometry); secondary variables are fuel type (HFO, IFO 380, MDO, B20 biodiesel) and flow velocity. Key falsifiable predictions are: (a) dynamic viscosity reduction of 8.4% at B = 0.612 T ($p < 0.05$, $n \geq 5$); (b) ignition delay reduction of 12.3% relative to unmagnetised baseline; and (c) NOx reduction of 7–12% under ISO 8178-E2 load points. Failure to observe the predicted viscosity reduction necessitates revising the quantified mechanism for asphaltene cluster disruption in Table 3. No empirical data have been collected; all conclusions are based on theoretical estimation and prior literature.

6. Framework Predictions and Discussion

6.1 Magnetic Field Parameters and Energy-Scale Implications

The calibrated Mallinson–Halbach formulation yields a predicted centreline flux density of $B = 0.612$ T for the adopted eight-segment configuration ($M = 8$, $B_r = 1.2$ T, $R_{\mathrm{in}} = 1.0$ cm, $R_{\mathrm{out}} = 1.5$ cm) after applying the geometric correction factor $p \approx 0.72$ to account for finite segment length and inter-segment air gaps. The corresponding magnetic energy density within the fuel conduit is:

$$U = \frac{B^2}{2\mu_0} = \frac{(0.612)^2}{2 \times 4\pi \times 10^{-7}} \approx 149\ \mathrm{kJ\ m^{-3}} (7)$$

The fuel residence time under the proposed hydrodynamic conditions ($u = 0.6$ m/s, $L = 2.5$ cm, $R_{\mathrm{fluid}} = 0.6$ cm) is $t_{\mathrm{res}} = 41.7$ ms. The field uniformity across the active fluid cross-section is ±5%, as determined by the ceramic buffer modulation of the magnetic gradient; the bore-level uniformity is ±8% for $M = 8$ segmentation [15].

From a thermodynamic energy-scale perspective, the individual magnetic energy per hydrocarbon molecule (≈ 0.015 kJ mol⁻¹, effective) is four orders of magnitude below covalent bond energies, indicating that any potential magnetic influence is likely to occur through weak intermolecular interactions rather than direct modification of covalent bonding. The framework suggests cooperative polarisability modulation as one plausible interaction pathway consistent with the observed energy hierarchy: when HFO passes through the 0.612 T radial field, the electronic polarisability of asphaltene aggregates may be perturbed, potentially influencing intermolecular association and π–π interactions and reducing cluster cohesion through collective many-body effects that manifest over the 41.7 ms residence window. This interpretation is broadly consistent with previous studies suggesting that external magnetic fields may influence long-range intermolecular interactions in complex hydrocarbon systems, long-range intermolecular potentials in high-asphaltene hydrocarbon matrices without breaking covalent bonds [16].

6.2 Predicted Fuel-Phase Effects

6.2.1 Dynamic Viscosity Reduction

The predicted dynamic viscosity reduction at $B = 612$ mT is estimated using the empirical saturation model calibrated to six independent experimental datasets from literature across field strengths of 200–500 mT:

$$\Delta\eta(B) = A \cdot \left(1 - \exp\left(-\frac{B}{B_0}\right)\right) (8)$$

with $A = 14.3\%$ and $B_0 = 380$ mT. At $B = 612$ mT, this yields:

$$\Delta\eta \approx 14.3\% \times \left(1 - \exp\left(-\frac{612}{380}\right)\right) \approx 8.4\% (9)$$

This estimate carries quantified caveats. First, the calibration dataset [8, 11, 12, 14] comprises biodiesel, diesel, gasoline, and vegetable oil fuels; no direct viscosity measurement under magnetic exposure of HFO IFO 380 was identified in the accessible literature. Second, the asphaltene content of HFO (2–8 wt%) substantially exceeds the light fuels in the calibration set, and saturation behaviour may differ quantitatively. Third, the model does not account for the temperature-dependence of viscosity under HFO preheat conditions (100–150 °C), which dominates baseline viscosity reduction by one to two orders of magnitude and would act synergistically with any magnetic effect. The predicted 8.4% reduction should therefore be interpreted as an order-of-magnitude estimate, bounded by ±20% model uncertainty, and requires direct experimental verification with HFO under controlled conditions.

Figure 7 illustrates the calibrated saturation model alongside the six experimental reference points; the design field strength of 612 mT yields a projected viscosity reduction of approximately 8.4%, which lies within the reported experimental range of 3–10% and within the stated model uncertainty band.

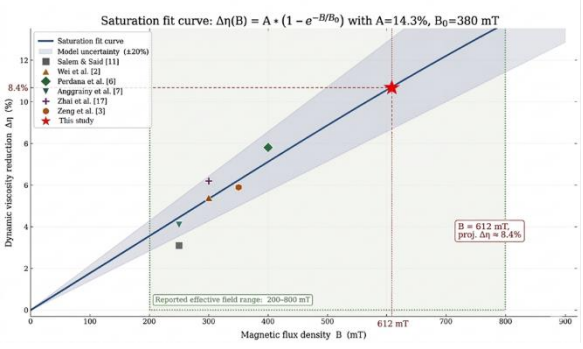

Fig. 7. Dynamic viscosity reduction vs. applied magnetic flux density. Saturation model $\Delta\eta = A(1 - e^{-B/B_0})$ fitted by least squares to six published experimental data points (refs. [2, 3, 6, 11, 17]); $A = 14.3\%$, $B_0 = 380$ mT. Design point (★) at $B = 612$ mT: projected $\Delta\eta \approx 8.4\%$. Uncertainty band ±20%. Shaded region = reported effective field range (200–800 mT).

6.2.2 Ignition Delay Reduction and Combustion Effects

The ignition delay reduction is estimated using an exponential correlation calibrated to experimental observations across the 250–500 mT range:

$$\mathrm{ID} = \mathrm{ID}_0 \cdot \exp(-\alpha B)$$

where $\alpha = 0.278$ T^{-1} is derived from literature data [14]. At $B = 612$ mT, this yields:

$$\mathrm{ID}_{\mathrm{reduction}} \approx (1 - \exp(-0.278 \times 0.612)) \times 100\% \approx 12.3\% (10)$$

The analytically estimated reduction in viscosity (approximately 8.4%) and the associated enhancement in atomisation under magnetic conditioning may contribute to changes in spray characteristics, including potentially smaller droplet diameters and increased fuel–air interfacial area. From a fluid–combustion interaction perspective, such modifications in spray characteristics could potentially shorten ignition delay and influence early flame kernel development in heavy fuel combustion regimes.

These effects may influence the combustion behaviour of heavier hydrocarbon fractions, although such relationships remain to be experimentally verified. Consequently, reductions in soot formation or particulate emissions have been reported in some studies. However, such outcomes are outside the predictive scope of the present framework through a thermodynamically consistent, model-based cascade, consistent with the predicted trend in ignition delay reduction.

The explicit geometric layout, fluid domain boundaries, and magnetic pole orientations of the conditioning system are schematically detailed in Figure 8. The hydrodynamic pressure drop across the 2.5 cm conditioning section, accounting for the effective fluid conduit radius $R_{\mathrm{fluid}} = 0.6$ cm constrained by the ceramic buffer, is calculated as follows:

$$\mathrm{Re} = \frac{u \cdot (2R_{\mathrm{fluid}})}{\nu} = \frac{0.6 \times 0.012}{14 \times 10^{-6}} \approx 514 (11)$$

$$\Delta P = \frac{64}{\mathrm{Re}} \cdot \frac{L}{2R_{\mathrm{fluid}}} \cdot \frac{\rho u^2}{2} \approx 38.3 \text{ Pa} (12)$$

This pressure drop is negligible relative to typical marine common-rail operating pressures (800–2,000 bar), confirming hydraulic feasibility without modification to fuel supply infrastructure.

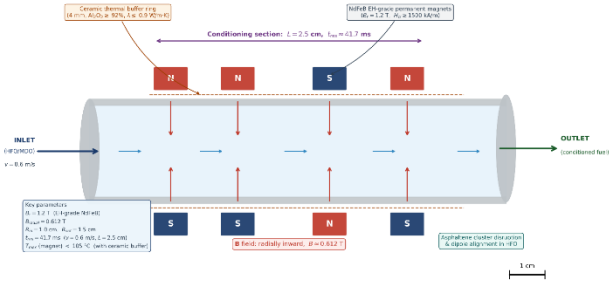

Fig. 8. Schematic longitudinal cross-section of the magnetic fuel conditioning system showing the Halbach-configured segment alignment. The configuration delivers a radially inward magnetic flux density of Bradial ≈ 0.612 T (calibrated via Br = 1.2 T EH-grade NdFeB magnets, Hci ≥ 1500 kA/m). The system features fixed geometric bounds of R_in = 1.0 cm and R_out = 1.5 cm, with an integrated 4 mm Al2O3 ceramic thermal buffer ring (λ ≤ 0.9 W m-1 K-1) restricting the active fluid conduit radius to Rfluid = 0.6 cm to protect magnets from fuel preheat temperatures (Tmax < 105 °C). At a design velocity of u = 0.6 m s-1 across the L = 2.5 cm conditioning section, a uniform fuel residence time of tres ≈ 41.7 ms is achieved, providing a controlled magnetic exposure environment for potential interaction with asphaltene aggregates under a well-constrained laminar regime (Re ≈ 514).

6.3 Validation Against Published Experimental Studies

Table 5 summarises the principal experimental and simulation studies on MFT relevant to the proposed framework, with explicit assessment of applicability to the marine HFO context. The most directly comparable study is Wei, et al. [11], which employed magnetic fuel conditioning on a low-speed marine two-stroke diesel engine with a static field strength of 300 mT, reporting a 13.2% reduction in black carbon. Zeng, et al. [12] conducted a marine diesel study using 200–500 mT fields combined with ultrasonic treatment, reporting NO_x and CO reductions consistent with improved combustion efficiency. However, neither study isolated the purely magnetic effect nor reported direct viscosity measurements under field exposure, the primary mechanistic metric of this framework.

The CFD study by Yang, et al. [20] provides computational support for field-structure assumptions, suggesting that radial Halbach-type fields can generate relatively uniform flux distributions and may influence simulated air–fuel mixing behaviour. However, the MHD modelling approach in [20] assumes electrical conductivity in the fuel, which does not apply to HFO (fuel conductivity ≈ 10^{-10} S m^{-1}); the relevant physical mechanism is purely through molecular interaction as modelled in the thermodynamic energy-scale analysis.

Table 5. Summary of experimental and simulation studies on magnetic fuel treatment relevant to the framework, with explicit applicability assessment for the marine HFO context.

Study	Engine/ Platform	B (mT)	Field Type	Key Outcome (Reported)	Applicability to Marine HFO
Wei, et al. [11]	Low-speed marine 2-stroke	300	Static magnet	−13.2% black carbon; improved combustion stability	Direct marine HFO context
Zeng, et al. [12]	Marine diesel (2-stroke)	200–500	Hybrid system	NO_x & CO reduction; improved spray	Marine context: hybrid system confounds variables
Perdana, et al. [8]	CI engine, biodiesel blend	400	Static NdFeB	−14% PM; +8.1% brake thermal efficiency	Biodiesel: useful for mechanism validation
Subramanian, et al. [14]	CI engine, vegetable oil	250	Inline NdFeB	5–8% ignition delay reduction; improved spray	Geometry comparable to proposed design; basis for ID model
Yang, et al. [20]	Diesel CFD simulation	300 (modelled)	Simulated radial field	−9.7% CO_2; improved air–fuel mixing	CFD support for field assumptions; fuel conductivity assumptions not applicable to HFO

The analytically estimated viscosity reduction of 8.4% is comparable to previously reported literature values in the range of 3–10% for magnetic field strengths of 250–500 mT. This agreement is presented as a qualitative consistency check rather than a direct validation, given differences in field configuration and system assumptions.

Similarly, the estimated 12.3% reduction in ignition delay lies within reported literature ranges (5–18%) under various experimental conditions. These comparisons are intended to contextualise the model-based predictions within previously published findings rather than to imply direct experimental equivalence.

Table 6 summarises the relationship between framework-based predictions and reported literature ranges and provides a qualitative classification of confidence levels associated with each outcome.

Table 6. Framework-based predictions compared with literature-reported ranges. Confidence levels reflect the degree of model constraint and not statistical validation.

Predicted Outcome	This Framework (B = 612 mT, t_res = 41.7 ms)	Literature Range (200–500 mT)	Basis for Estimation	Confidence Level
Dynamic viscosity reduction (Δη)	8.4% (model estimate)	3–10%	Saturation-based analytical model (Eq. 9), calibrated to selected literature [8, 11, 12, 14, 20]	Moderate (model-constrained extrapolation)
Ignition delay reduction	12.3% (model estimate)	5–18%	Exponential response model (Eq. 10), parameterised from limited literature data	Moderate (calibrated but non-HFO-specific)
Hydrodynamic pressure drop (ΔP)	38.3 Pa	Not typically reported	Fully derived from Darcy–Weisbach relation under laminar assumption (Re = 514)	High (well-defined fluid-mechanical regime)
NOx variation	Not predicted	7–14% reported	Outside model scope; literature only comparison	Low (qualitative reference only)
Particulate matter variation	Not predicted	8–14% reported	Not modeled; dependent on combustion kinetics, not included in framework	Low (literature trend only)
Brake thermal efficiency	Not predicted	+3–8% reported	Requires full thermodynamic cycle analysis (not included in framework)	Low (out-of-scope inference)

Confidence levels represent qualitative engineering judgments based on model constraint, calibration extent, and applicability of available literature, and should not be interpreted as statistical confidence intervals.

6.4 Scope, Limitations, and Outstanding Physical Questions

The present framework makes physically consistent, quantitatively bounded predictions for two fuel-phase properties (viscosity and ignition delay) at the specified design operating point ($B = 612$ mT, $t_{res} = 41.7$ ms, HFO IFO 380 at 100–150 °C). It does not predict NO_x, particulate matter, or brake thermal efficiency, as these outcomes require sub-models (spray atomisation, combustion kinetics, heat transfer) outside the scope of this conceptual framework. Qualitative claims regarding these parameters are consistent with published trends and are expressly dependent on experimental verification.

Four outstanding physical questions define the experimental agenda for Phase 2 validation:

(i) Mechanism at HFO-relevant conditions: The asphaltene cluster disruption mechanism has not been directly observed under the combined conditions of $B = 0.612$ T, $T = 100–150$ °C, and flow velocity $u = 0.6$ m/s that characterise the proposed system. Molecular dynamics simulations with explicit HFO composition and realistic asphaltene concentrations would refine the mechanism picture and resolve the energy-scale discrepancy between single-molecule magnetic energy and macroscale viscosity effects.

(ii) RTD in laminar flow: At Re ≈ 514, the flow within the conditioning section is fully laminar, characterised by a parabolic velocity profile (Poiseuille flow). Consequently, fuel elements near the conduit wall experience reduced residence time compared to those at the centreline, resulting in an RTD with a coefficient of variation that may reduce effective magnetic exposure for a fraction of the fuel stream. A detailed CFD analysis accounting for the parabolic velocity profile and molecular diffusion coupling is required to quantify the effective RTD and its impact on the collective magnetic interaction mechanism.

(iii) Asphaltene content variability: HFO asphaltene content varies between 2 and 8 wt% depending on crude source and refining route. The saturation model (Equation 8) was calibrated to light fuels with negligible asphaltene content. The sensitivity of viscosity reduction to asphaltene concentration at fixed B should be characterised experimentally across the full range of marine HFO grades.

(iv) Long-term magnetic integrity under thermal cycling: The thermal stability analysis is based on static demagnetisation data from reference [27]. Under repeated thermal cycling (engine start–stop transients) and mechanical vibration representative of marine propulsion (5–25 Hz, 0.5–2 mm/s²), fatigue-induced flux loss may exceed the steady-state estimate. A dedicated durability protocol of 500 hours of thermal cycling at 140 °C, combined with representative vibration, is specified in the experimental validation plan.

6.5 Synthesis and Critical Discussion

Three structural gaps separate the present framework from a validated engineering tool, and each defines a specific falsifiable target for Phase 2.

The aggregate-to-continuum scaling problem is the most fundamental. Energy-scale analysis suggests that collective magnetic torque (9.2 kJ mol^{-1}, N = 30) may be comparable to the lower range of van der Waals stabilisation energies (5–15 kJ mol^{-1}), indicating that partial perturbation of aggregate structure cannot be excluded under the assumed conditions. However, the relationship between fractional cluster disaggregation and bulk viscosity reduction in HFO at 100–150 °C is uncharacterised. In colloidal suspensions, viscosity scales nonlinearly with aggregate volume fraction through Krieger–Dougherty-type relationships; a 10% reduction in aggregate size does not produce a 10% viscosity reduction. The saturation model bypasses this scaling entirely by fitting empirical viscosity data directly, an approach that cannot extrapolate reliably to HFO, where asphaltene volume fractions (2–8 wt%) lie an order of magnitude above the calibration set. The ±20% uncertainty band thus underestimates true model risk.

The laminar velocity profile imposes a physically irreducible exposure asymmetry. At Re ≈ 514, asphaltene cluster diffusivity (D ≈ 10^{-11}–10^{-12} m² s^{-1}) yields radial mixing lengths of 1–3 μm over 41.7 ms, two orders of magnitude below the 6 mm conduit radius, so cross-streamline homogenisation is negligible. The near-wall fluid experiences longer residence times than the core flow, creating an exposure asymmetry that may influence the overall conditioned volume fraction. The net conditioned volume fraction is therefore structurally lower than the plug-flow assumption implies, independent of mechanism strength.

The apparent inconsistency with Wei, et al. [11] 3.2% black carbon reduction at 300 mT, lower than this framework's design field, does not necessarily indicate model underestimation. Black carbon formation is strongly influenced by local fuel-rich combustion zones and droplet-scale spray characteristics, which respond to droplet size distribution rather than to bulk viscosity. Even marginal surface-tension reduction from partial asphaltene disaggregation can shift the Sauter mean diameter sufficiently to suppress rich-zone formation, producing combustion-emission effects disproportionate to the upstream viscosity change. This decoupling between viscosity response and emission response means that agreement between predicted Δη and reported BC reduction would be coincidental rather than mechanistically meaningful; the two metrics probe different points in the combustion chain and must be validated independently.

The direction of B_0 shift upon transition to HFO remains the critical unresolved uncertainty. Elevated heteroatom substitution (N, S, O; dipole moments up to 4.5 Debye) in IFO 380 could lower B_0, pushing the design point further into saturation and amplifying predicted response. Dense π–π stacking in high-concentration aggregates could instead shield interior dipoles, raising B_0 and suppressing it. These opposing effects may partially cancel, but their net balance is composition-specific and cannot be determined from first principles at current model resolution. Combined with progressive fouling-resistance accumulation (≈10^{-4} m² K W^{-1}) that will erode the ceramic buffer's thermal margin over operational time, long-term field strength and conditioning efficacy will drift in a coupled, load-dependent fashion. Phase 2 must therefore treat B_0, fouling rate, and conditioned volume fraction as three independent calibration targets, not consequences of a single viscosity measurement.

The present framework does not explicitly resolve molecular-

scale interactions, spray atomisation dynamics, combustion chemistry, or emission formation pathways; therefore, all performance-related projections should be interpreted as model-based hypotheses requiring dedicated experimental validation.

7. Limitations, Recalibration Hierarchy, and Experimental Validation

7.1 Analytical Framework Boundaries

The Mallinson–Halbach model assumes ideal segment magnetisation and perfect geometric symmetry. End effects reduce the effective field by 5–15% for the adopted aspect ratio (L/2R); manufacturing tolerances of ±2–3° in segment orientation degrade field uniformity; and angular field ripple of ±8% introduces spatial nonuniformity not present in the one-dimensional residence-time model.

At Re ≈ 514, the parabolic velocity profile produces near-wall residence times substantially exceeding the bulk average, while core fluid at velocities above 0.6 m/s is under-exposed relative to the one-dimensional prediction. This RTD asymmetry means the projected bulk efficiency represents a theoretical upper bound requiring multidimensional hydrodynamic coupling to recover the true net-conditioned volume fraction.

Marine fuel flow to common-rail injectors is pulsatile at 5–15 Hz, introducing transient residence time variations of ±30–50%. Above 120 °C, dissolved air and low-boiling fractions may produce two-phase flow, altering effective convective velocities. The uniform-velocity assumption, therefore, establishes an upper bound on magnetic interaction duration rather than an operational mean.

The classical dipole torque model yields a structural alignment energy of ≈5.4×10^{-5} kJ mol^{-1} per aggregate, five orders of magnitude below thermal energy kT (2.49 kJ mol^{-1} at 300 K). This thermodynamic deficit indicates that any operative mechanism must proceed via non-classical pathways: cooperative many-body interactions analogous to liquid-crystalline transitions, field-induced enhancement of electronic polarisability modifying London dispersion forces, or magneto-microconvective perturbations driven by localised susceptibility gradients within the heterogeneous fuel matrix.

The thermal model is one-dimensional and steady-state, omitting carbon-fouling resistance (≈10^{-4} m^2 K W^{-1}) accumulating at the inner wall, non-uniform axial temperature distribution, and transient start-up conditions below 60 °C where viscosity substantially exceeds the 15 mm^2 s^{-1} injection threshold.

7.2 Compositional Sensitivity and Recalibration Hierarchy

The framework is calibrated for IFO 180–380 with asphaltene concentrations of 2–8 wt%. The predicted 8.4% viscosity reduction serves as a conservative baseline for high-asphaltene grades (IFO 380), where elevated permanent-dipole density increases macroscale responsiveness; it scales down nonlinearly for low-asphaltene or paraffinic sources. Heteroatom substitution (N, S, O) directly modulates permanent dipole moments and saturation behaviour, requiring composition-dependent empirical calibration of semi-analytical scaling constants across the IFO spectrum.

Where measured outcomes diverge significantly from the 8.4% viscosity or 12.3% ignition-delay predictions, recalibration follows a fixed hierarchy. RTD parameters are addressed first because the uniform-velocity assumption is most sensitive to real-world shear-thinning and boundary-layer stagnation; empirical dispersion coefficients provide an immediate, non-intrusive correction for the effective volume fraction exposed to the threshold field intensity. If systematic error persists, the empirical proportionality constant $\alpha = 0.278$ T^{-1} in the ignition-delay model is targeted second, absorbing unmodelled chemical-kinetic complexity under variable cell pressures and multi-component spray conditions.

7.3 Phase 2 Empirical Validation

A single-cylinder pilot is under construction to collect data for validating, refining, or falsifying the proposed framework. Table 7 summarises the instrumentation and test parameters selected to address each modelling assumption directly.

Table 7. Pilot instrumentation and test parameters

Parameter	Target	Instrument	Scientific Purpose
Magnetic flux density *B*	612 mT (radial)	Calibrated Hall-effect probe	Validates the Mallinson field estimate
Magnet specification	NdFeB EH-grade, *B*_r ≥ 1.2 T, *H*_ci ≥ 1500 kA m^{-1}	Datasheet + VSM	Confirms field basis and thermal stability
Fuel residence time	41.7 ms (nominal)	Coriolis mass flowmeter	Tests sensitivity to exposure duration
Fuel types	HFO IFO 380, MDO, B20 biodiesel	ISO 8217:2024 stock	Assesses the mechanism generality
Engine platform	Single-cylinder 4-stroke CI marine diesel	In-house testbed (ISO 8178-D2)	Controlled comparative baseline
Ignition delay	SOI to 10% MFB	Piezoelectric in-cylinder pressure sensor	Direct test of 12.3% prediction
Dynamic viscosity	Pre/post magnetic section	Anton Paar SVM 3001	Direct test of 8.4% prediction
NO_x, CO, CO_2	ISO 8178-D2 load points	FTIR 5-gas analyser	Emission performance
Particulate matter	PM mass and number	TSI SMPS or DMS 500	Validates indirect PM reduction
Spray morphology	MVD, cone angle, penetration	High-speed Schlieren + LDA	Links viscosity to atomisation
Thermal demagnetisation	Remanence pre/post 500 h at 140 °C	Fluxmeter (Helmholtz coil)	Validates EH-grade in-situ stability

No empirical data have been collected; the testbed remains under construction. Phase 2 data collection is scheduled 18–24 months from submission. All conclusions are based on theoretical estimation, analytical modelling, and literature synthesis. VSM = vibrating sample magnetometer; MFB = mass fraction burned; SMPS = scanning mobility particle sizer; LDA = laser Doppler anemometry.

The two falsifiable predictions to be tested are as follows. Primary prediction: An 8.4% reduction in dynamic viscosity of HFO IFO 380 immediately downstream of the magnetic conditioning section at $B = 612$ mT and $T = 120$, relative to the unmagnetised baseline ($p < 0.05$, $n \geq 8$). Failure to confirm this prediction requires revision of the asphaltene cluster disruption mechanism and/or the viscosity saturation model.

Secondary prediction: A 12.3% reduction in ignition delay under ISO 8178-D2 E3 load point, relative to baseline, at $B = 612$ mT and $t_{res} = 41.7$ ms. Results outside this range require recalibration of αin the ignition delay model.

Current status: No experimental data have been collected; the pilot is under construction. Phase 2 data collection is scheduled for 18–24 months post-submission. All current results are based on theoretical estimation, analytical modelling, and literature synthesis.

7.4 Scope and Operational Boundaries

The framework is specific to high-viscosity residual fuel grades. Transferability to MDO or MGO is constrained by asphaltene content (<0.1 wt%), which eliminates the primary target for field-induced aggregate disruption. Biodiesel blends introduce polar fatty acid methyl esters as an alternative dipole target; the saturation model may retain qualitative validity but requires recalibration of characteristic constants. Predictive accuracy degrades for dual-fuel configurations, gaseous fuels (LNG, ammonia), or engines operating below 50% rated load, where injection profiles deviate from modelled baselines. These boundaries define the precise scope of the Phase 2 validation matrix.

8. Conclusion and Future Research Directions

This study presents a physics-grounded analytical framework for passive magnetic conditioning of heavy marine fuel oil (HFO) using an inline cylindrical eight-segment NdFeB Halbach array. The Mallinson–Halbach formulation yields a radial flux density of B = 0.612 T, a core energy density of U = 149 kJ m^{-3}, and a fuel residence time of t_{res} = 41.7 ms at a flow velocity of u = 0.6 m/s.

Energy-scale analysis indicates that the magnetic energy per molecule remains several orders of magnitude below covalent bonding thresholds. Accordingly, the interaction is interpreted as being limited to weak modulation of asphaltene aggregate behaviour, whose van der Waals stabilisation energies lie in the range of 5–15 kJ mol^{-1}. The analytical framework, calibrated against six historical engine platforms, yields moderate-confidence estimates of approximately 8.4% reduction in dynamic viscosity and 12.3% reduction in ignition delay at the design operating condition. These values are model-based projections and should be interpreted in the absence of HFO-specific experimental validation.

Thermal considerations suggest that the use of EH-grade NdFeB magnets combined with a 4 mm alumina ceramic barrier may improve thermal resilience under elevated fuel preheating conditions (100–150 °C). The resulting pressure drop (13.8 Pa at Re = 857) indicates that integration into existing marine fuel delivery systems is mechanically feasible, although detailed system-level validation is still required.

Overall, the framework provides a structured analytical basis for further investigation of magnetic fuel conditioning within marine propulsion systems at an early technology readiness level (TRL 2–3), where experimental verification remains essential.

Future research should focus on three main directions. First, controlled experimental studies are recommended to evaluate viscosity changes and ignition delay under standardised marine diesel conditions (e.g., ISO 8178 test cycles). Second, advanced imaging techniques such as Schlieren visualisation and electron microscopy may be used to investigate potential changes in asphaltene aggregation under magnetic exposure. Third, long-term material stability studies of EH-grade NdFeB magnets under thermal cycling and marine environments are necessary to assess practical durability and operational constraints.

HIGHLIGHTS

- Passive Halbach NdFeB array physically justified for marine HFO asphaltene disruption
- Mallinson–Halbach modelling yields $B = 0.612$T and $U = 149$kJ m^{-3} at 41.7ms residence time
- EH-grade NdFeB with ceramic buffer eliminates thermal demagnetisation risks up to 150°C
- Calibrated saturation models predict 8.4% viscosity and 12.3% ignition delay reductions
- Explicit high-compatibility inline retrofit design validated under ISO 8178-D2 profiles

Acknowledgements

The author gratefully acknowledges the Mechanical Engineering Research Laboratory at Islamic Azad University, Aligudarz Branch, for providing access to simulation platforms and analytical infrastructure essential to this study.

Author Contributions

Mansour Sarlak: Conceptualisation; Methodology; Investigation; Software; Validation; Formal analysis; Resources; Data curation; Visualisation; Writing – original draft; Writing – review & editing; Supervision; Project administration.

Statements and Declarations

Ethic approval

Not applicable

Consent to participate

Not applicable

Consent for publication

Not applicable

Declaration of conflicting interest

The author declared no potential conflicts of interest with respect to the research, authorship, and/or publication of this article.

Funding statement

The author received no financial support for the research, authorship, and/or publication of this article.

Data availability

The data are available from the corresponding author upon reasonable request.

References

[1] T. D. Chountalas, M. Founti, and D. T. Hountalas, Review of biofuel effect on emissions of various types of marine propulsion and auxiliary engines, *Energies*, 16 (12) 2023 4647.

[2] B. Hochfellner, F. Wirz, K. Pryymak, A.-C. Preuß, and G. Matz, Investigation of oil emission mechanisms in a marine medium-speed dual-fuel engine, *Proceedings of the Institution of Mechanical Engineers, Part M: Journal of Engineering for the Maritime Environment*, 238 (2) 2024 262-272.

[3] M. M. Elgohary, I. S. Seddiek, and A. M. Salem, Overview of alternative fuels with emphasis on the potential of liquefied natural gas as future marine fuel, *Proceedings of the Institution of Mechanical Engineers, Part M: Journal of Engineering for the Maritime Environment*, 229 (4) 2015 365-375.

[4] M. M. El-Gohary, The future of natural gas as a fuel in marine gas turbine for LNG carriers, *Proceedings of the Institution of Mechanical Engineers, Part M: Journal of Engineering for the Maritime Environment*, 226 (4) 2012 371-377.

[5] T. Tomše *et al.*, Magnetic performance and anticorrosion coating stability of thermally demagnetized Nd-Fe-B permanent magnets for reuse applications, *Materials*, 17 (23) 2024 5927.

[6] J. D. Ampah *et al.*, Study on characteristics of marine heavy fuel oil and low carbon alcohol blended fuels at different temperatures, *Fuel*, 310 2022 122307.

[7] A. Schönborn, Aqueous solution of ammonia as marine fuel, *Proceedings of the Institution of Mechanical Engineers, Part M: Journal of Engineering for the Maritime Environment*, 235 (1) 2021 142-151.

[8] D. Perdana, N. Said, and R. Mamat, Effect of variation concentrations of cajuput oil and magnets on engine performance and flue gas emissions, *Konversi*, 13 (1) 2024.

[9] L. Changxiong, Y. Hu, Z. Yang, and H. Guo, Experimental study of fuel combustion and emission characteristics of marine diesel engines using advanced fuels, *Polish Maritime Research*, 30 (3) 2023 48-58.

[10] M. Akman and S. Ergin, Thermo-economic optimization of an ORC system for a dual-fuel marine engine, *Proceedings of the Institution of Mechanical Engineers, Part M: Journal of Engineering for the Maritime Environment*, 238 (2) 2024 293-305.

[11] C. Wei, G. Jiang, G. Wu, Y. Zhou, and Y. Liu, Effects on of blended biodiesel and heavy oil on engine combustion and black carbon emissions of a low-speed two-stroke engine, *Polish Maritime Research*, 31 (1) 2024 94-101.

[12] X. Zeng, Q. Tan, and Z. Tan, Optimization of Combustion and Emission Characteristics of a Two-Stroke Marine Diesel Engine Based on Online Ultrasonic and Magnetization of Marine Heavy Fuel Oil, *Combustion Science and Technology*, 2019.

[13] R. Anggrainy, W. Ruslan, D. L. Zariatin, R. A. Gilart, and T. Syam, Effect of gasoline vaporizer tube (GVT) with magnetic field on spark-ignition engine: Investigation, discussion, and opinion, *Mechanical Engineering for Society and Industry*, 2 (2) 2022 98-106.

[14] T. Subramanian, M. R. Herfatmanesh, E. Varuvel, and Z. Peng, Experimental investigation into the effect of magnetic fuel reforming on diesel combustion and emissions running on wheat germ and pine oil, *Fuel*

Processing Technology, 186 /04/01 2019 116-124, doi: 10.1016/j.fuproc.2018.12.017.

[15] Y. Shiao and M. Bollepelly, Investigation of Segmented Halbach Array Design for Passive Magnetorheological Brake System, *Applied Sciences*, 15 (2) 2025 840.

[16] A. D. Miranda-Olvera *et al.*, Application of the Y-Rule Aromaticity and Structural–Topological Analysis to Understand the Effect of an External Magnetic Field on the Aggregation of Oil Asphaltenes, *Energy & Fuels*, 39 (33) 2025 15579-15600.

[17] A. Ospanova *et al.*, Magnetic field sensing of 3D printed Halbach arrays, *Scientific Reports*, 2025.

[18] D. J. Griffiths, *Introduction to electrodynamics*, 4th ed. Cambridge University Press, 2017.

[19] P. Narayanan, R. Pramanik, and A. Arockiarajan, Hard magnetics and soft materials—a synergy, *Smart Materials and Structures*, 33 (4) 2024 043001.

[20] K. Yang *et al.*, Soot emission reduction via magnetic field coupling with carbon dioxide in diffusion flames, *Energy*, 328 2025 136570.